University of Groningen

Medusa Radiometrics

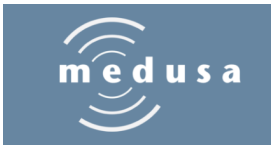

Bachelor's project

Searching for weak radioactive sources with a drone

Author:
Jesse Rolfes *(S3429709)*

Supervisors:
dr. Emiel van der Graaf
dr. Catherine Rigollet
Steven van der Veeke

July 3, 2020

Abstract

A theoretical model for source detect ability at various distances was created and experiments with a 12.8 ml CeBr3 detector mounted under a DJI Phantom 4 as well as a 350 ml CsI detector mounted under a DJI Matrice 600 pro were performed. It was concluded that detecting a 1.3 MBq source is possible, as well as locating it, although the GPS error limited the precision to several meters. It was also found that the sensitivity of the detector decreases when the fly speed increases and that a combination of count rate and peak area counts give the best change for detecting a source.

Contents

1 Introduction

Radioactive sources can be lost or stolen, for example: in the United Kingdom, there were more then 30 incidents with lost radioactive sources in a time period of 10 years [1]. These lost radioactive sources form a risk for humans and the environment in general, therefore it is essential that these sources get located as soon as possible. Locating the source can be done by deploying mobile radiation sensing systems in the suspicious area. This mobile system can consist of a gamma ray detector carried by a human, mounted on a car, placed in a helicopter or flown by a drone. Of these options a drone stands out because of the benefits it overs:

- A drone is remotely controlled, which minimizes human risks.
- A drone flies, enabling easy access to difficult terrain for humans on foot or in a car.
- A drone can fly at lower heights then other (unmanned) airborne methods such as helicopters, so more detailed information can be gathered.
- A drone is cheaper then other (unmanned) airborne methods, such as helicopters or planes, improving accessibility to the technology.

However the use of a drone also has some drawbacks, one of which is it's low carrying weight with respect to other methods. This results in a need for light weight and therefore small detectors, which have in general worse properties then big detectors. The goal in this project is to understand what the capabilities of a small detector, that fits under a drone, are, when trying to locate a weak source. So a theoretical model for source detect ability was created in python and based on these predictions a set of experiments were conducted. These experiments tested the predictions of the model and the capability of the drone to locate a source.

2 Gamma spectrometry[1]

In this project the focus is on finding a gamma ray source with a small gamma ray detector under a drone. With this in mind it is important to understand the workings of gamma spectroscopy. Therefore the way in which gamma rays interact with matter and where they originate from will be briefly explained.

Gamma rays are part of the electromagnetic spectrum and are located at the high energy side of this spectrum, with energies of about 10 keV and higher. Gamma rays can be created when transitions between excited states of nuclei occur. These nuclei are excited as a consequence of decay reactions, which include: β^- decay, β^+ decay and α decay. Other sources of gamma radiation include: positron-electron annihilation, Bremsstrahlung and prompt gammas.

When gamma rays are emitted via a nuclear transition or annihilation process they are mono-energetic. With their energy being equal to the difference in the energy levels of the nucleus, in the case of nuclear transitions. For the case of annihilation two gamma rays will be emitted back-to back and the energy of each gamma ray is equal to the electron rest energy (511 keV). Because of the uniqueness of the energy levels within nuclei, the gamma rays emitted are characteristic for certain radionuclides. Thus, when the energy of these gamma rays can be measured precisely the nuclei could be identified. This is the basic concept of gamma ray spectroscopy.

To be able to analyze the gamma rays that are emitted they need to be detected. This can be done via the interactions that gamma rays have with matter. The interactions that can occur are: the photoelectric effect, Compton scattering and pair production.

The photoelectric effect occurs when a gamma ray interacts with a bound electron of the absorbing material. The gamma ray is completely absorbed and as a consequence a photo-electron is ejected, see figure 1. This leaves a vacancy in one of the bound electron shells of the atom, which can be filled by capturing a free electron in the medium and/or by rearranging the electrons from the other shells. The rearrangement of the electrons releases x-rays that are usually captured by neighboring atoms in the same way, but they could also escape the material.

[1] All the information below is based on [2] unless stated otherwise.

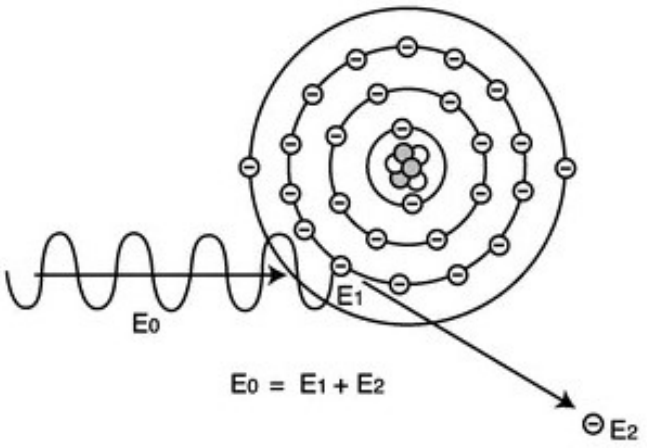

Figure 1: The photoelectric effect where E_0 is the gamma ray energy, E_1 is the binding energy of the electron and E_2 is the electron energy [3].

Compton scattering happens when a gamma ray scatters on an electron, in the absorbing material. The gamma ray is reflected at an angle θ to its original travel direction, see figure 2. A portion of the energy of the gamma ray is transferred to the electron, the exact amount of energy transferred varies, since it depends on the angle θ.

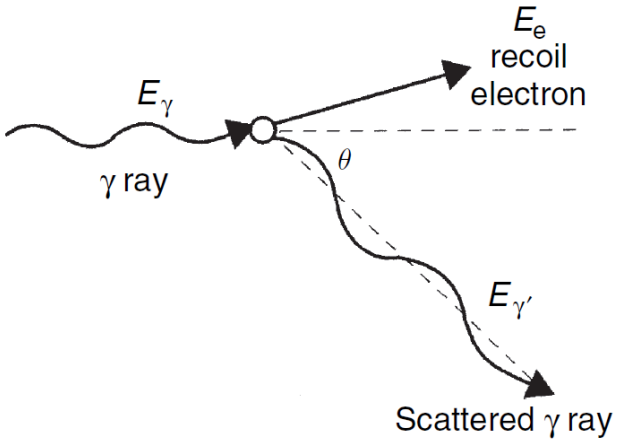

Figure 2: A depiction of Compten scattering, where E_γ is the gamma ray energy and E_e is the energy of the electron [2].

Pair production only takes place when the energy of the gamma ray exceeds the rest energy of two electrons, which is 1022 keV. The interaction needs to take place in the Coulomb field of a nucleus. When it happens the gamma ray gets converted into an electron and positron pair, see figure 3. The energy of the gamma ray above 1022 keV, becomes kinetic energy that is divided between the two particles. The positron that is created will annihilate when it has slowed down in the material, releasing two annihilation photons.

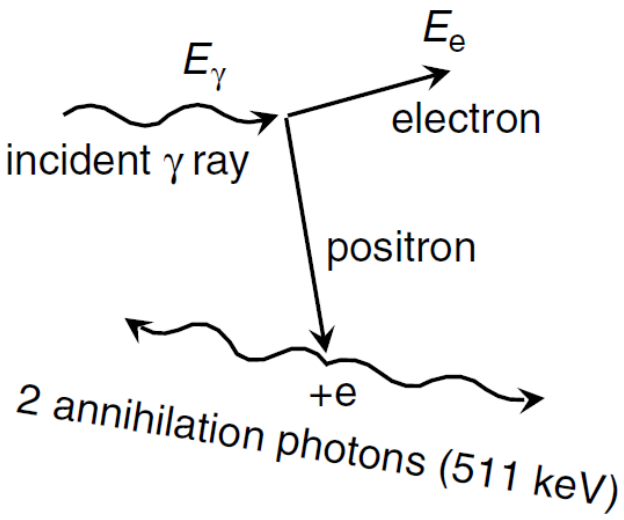

Figure 3: The process of pair production where E_γ is the gamma ray energy and E_e is the electron energy. Also the process of positron-electron annihilation giving rise to two 511 keV gamma rays is shown [2].

2.1 Detectors[2]

Via the interactions explained in the section above, all or a part of the energy of the gamma ray, is deposited into the material where it interacts with. This deposited energy can be recorded and used to create a spectrum. In a spectrum the pulse amplitude or amount of energy recorded is displayed, usually via the differential pulse height distribution. This means that the number of pulses dN within an small energy window dE, are divided by that window and displayed. It follows that by integrating the graph the number of counts is obtained.

In an ideal case all energy of every gamma ray would be deposited and only peaks at that energy would occur, but in reality some energy of the gamma ray could escape and a continuum of energies is recorded, up to a maximum energy equal to the most energetic rays that are present. Some of the ways in which energy is lost can show as specific peaks in a spectrum as can be seen in figure 4.

[2]The information in the following section was retrieved from reference [4].

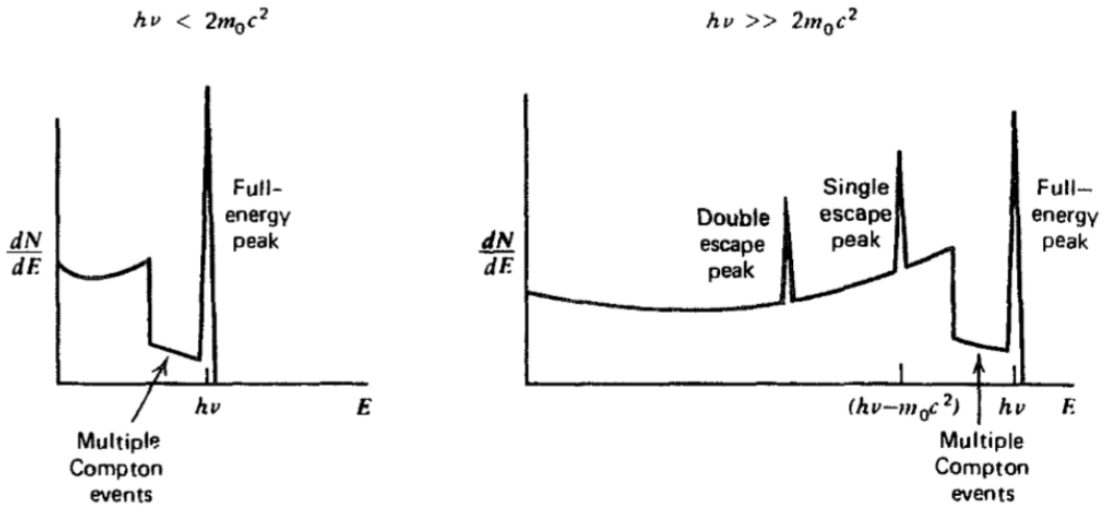

Figure 4: At the left of both spectra there is the continuum from single Compton scattering followed by multiple Compton scattering and then the full energy peak. Only in the right spectrum two additional peaks from the escape of either one or two annihilation photons are present, since the energy of the gamma ray producing the full energy peak, is high enough for pair production.[4]

Some general properties of a gamma ray detector include: their operating mode, their energy resolution, their detection efficiency and their dead time behaviour.

The operating mode describes the way in which the signal is interpreted. Most detectors are used in pulse mode, because it is the most effective at retaining information on the amplitude and timing of the gamma rays.

The energy resolution relates to the ability of the detector to distinguish gamma rays of different energies. The resolution is defined with the help of the full width at half maximum (FWHM), which is the width of the peak at half the height. In this definition it is assumed that there is no background radiation in the data. Then the energy resolution is given by: FWHM/H_0, here H_0 is the centroid of the peak. In figure 5, both a peak with a good and a poor energy resolution is shown.

A higher resolution detector will be able to better distinguish peaks, that are close to each other in energy. A general rule for this is that two peaks should be more then one FWHM apart to resolve them. Therefore, the resolution of a detector could be important if one wants to identify which radionuclides are present, since the characteristic peaks are more prevalent.

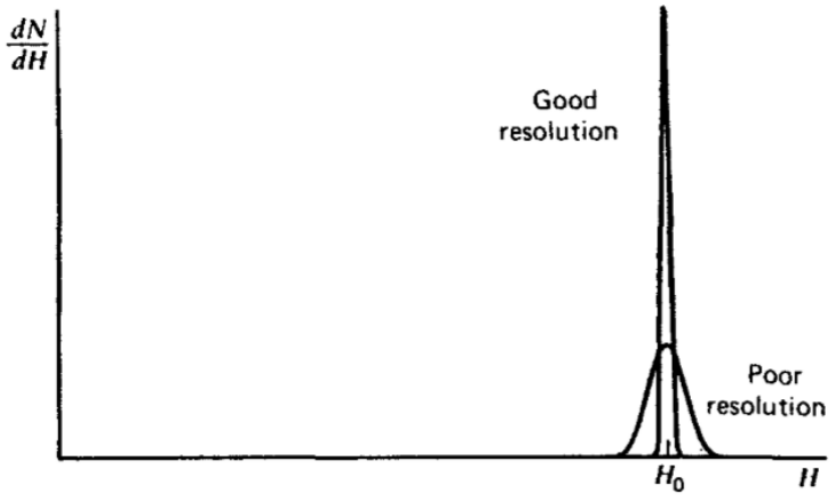

Figure 5: The broader peak represents a poor energy resolution since the recorded events spread over a wider energy range, compared to the good energy resolution peek [4].

The detection efficiency states how well the detector can detect gamma rays. It relates the counted gamma rays to the actual amount of gamma rays incident on the detector. This is know as the intrinsic efficiency ϵ.

$$\epsilon = \frac{\text{counted gamma rays}}{\text{gamma rays incident on the detector}} \tag{1}$$

The dead time τ describes the finite amount of time a detector needs to process a single event. A consequence of this process time is the possibility of missing an event, since one could occur when the detector is processing. However, this only becomes a problem at high count rates, where the true interaction rate n is bigger than $1/\tau$. At low interaction rates $n << 1/\tau$ the dead time will not be a significant part of the measurement and can be corrected for, with the help of the following relation:

$$m \approx n(1 - n\tau). \tag{2}$$

Here m is the counts registered by the detector.

Above some general detector properties are discussed and the following section will be specifically about scintillation detectors, since these will be used in the analysis later in this report.

In a scintillation detector the gamma ray interacts with the scintillation crystal. As a consequence the crystal will emit scintillation photons. These photons will be in, or near the optical wavelength and are proportional to the energy deposited by the gamma ray. This light is then collected to create an electrical signal. The light can be transformed into an electrical signal in two different ways. It can be done with a photomultiplier tube(PMT) or with a photodiode[2].

When a PMT is used the light strikes a photocathode releasing photoelectrons. These electrons are multiplied in an electron multiplier structure. After sufficient amplification the electrons are collected on the cathode and the amplitude of the resulting voltage pulse, is proportional to the energy deposited in the crystal. In figure 6 the general arrangement of a scintillation detector with PMT is shown.

When a photodiode is used the light of the scintillation crystal can be directly collected on it and converted into a voltage pulse. In figure 7 the configuration of such scintillation detector with photodiode is shown.

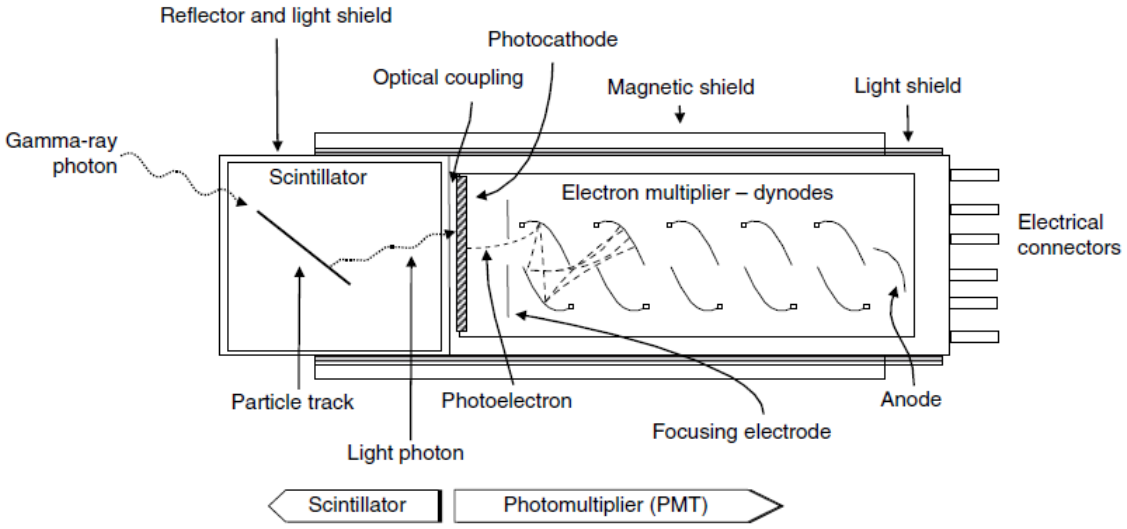

Figure 6: A schematic drawing of a scintillation detector with a PMT[2].

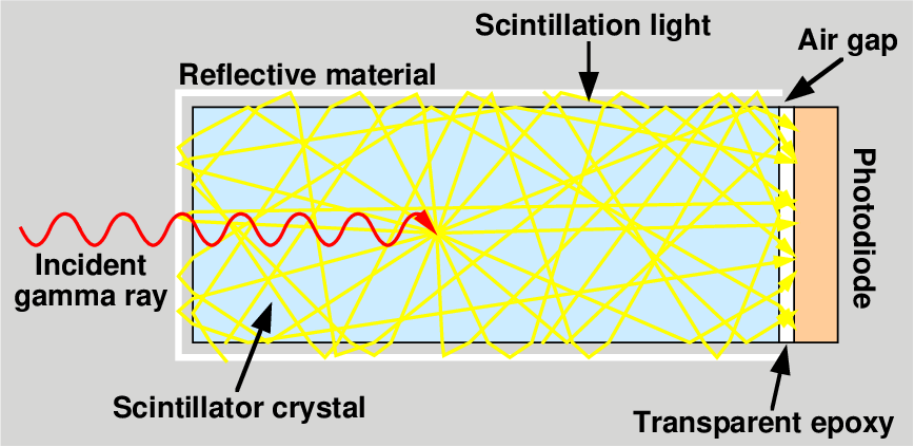

Figure 7: A schematic drawing of a scintillation detector with a photodiode[5].

2.2 Background radiation

When doing radiation measurements it is important to consider the background radiation since this needs to be subtracted from the measurement to get a meaningful result.

In the the natural environment there are a lot of elements with radioactive isotopes, but only a few of them are abundant enough and emit radiation with energies high enough that they can be readily detected.

These radioisotopes include: ^{40}K, ^{235}U, ^{238}U and ^{232}Th. Potassium ^{40}K decays to Argon via electron capture and emits an 1460 keV gamma ray, in about 11% of the cases. While it decays to Calcium via β^--decay 89% of the time[6]. The other radioisotopes are the head of a decay series that terminates at a stable isotope of lead, these are shown for ^{238}U and ^{232}Th in figure 8 and 9. The decay serie of ^{235}U is not shown, because the natural occurring uranium is comprised for 99.3% of ^{238}U by weight[7]. Therefore the presence of ^{235}U is ignored.

The most prominent gamma rays emitted by the natural occurring elements are 1460 keV, 1765 keV and 2614 keV. These are emitted by ^{40}K, ^{214}Bi and ^{208}Tl respectively. Here, ^{214}Bi and ^{208}Tl are daughter nuclides of ^{238}U and ^{232}Th respectively.

The activity of natural nuclides in the Dutch soil has been mapped and the concentrations found are listed in table 1.

Table 1: A table listing the concentrations of ^{40}K, ^{238}U and ^{232}Th in the ground of the Netherlands [8].

Radionuclide	Radioactivity concentration range (Bq/kg)	Typical concentration (Bq/kg)
^{232}Th	10-80	25
^{238}U	5-100	25
^{40}K	100-700	400

The spectra of the natural occurring isotopes can be generated by a Monte Carlo simulation and can be used to fit a background spectrum measurement. The parameters of this fit determine their relative contributions. This way of examining gamma ray spectra is called full spectrum analyses [9].

When considering the background radiation it is also important to consider the terrain and weather when measuring, since it can significantly attenuate the radiation. For example, rain fall can decrease the fluence rate by about 10 percent when the soil moisture content increases with the same percentage. Rain can also cause precipitation of radon daughter nuclei, since these nuclei attach to dust particles. This precipitation can cause an apparent increase of 2000 percent in uranium ground concentration. Therefore no measurements should be taken during or right after rain. There is about 3 hours needed for the radon to evaporate and disperse, after which the effect disappears. [10].

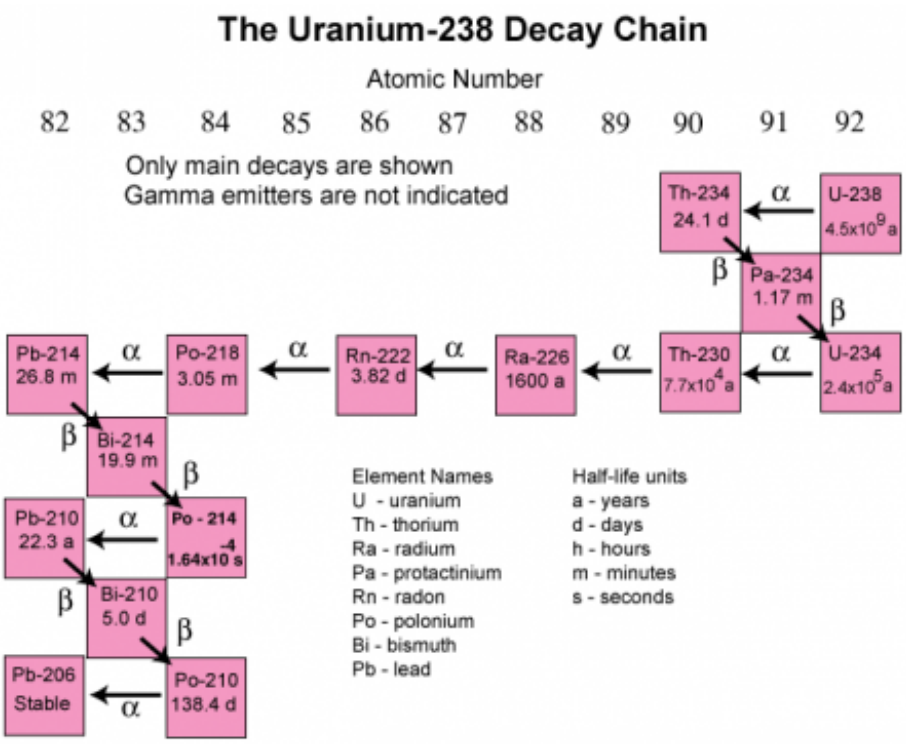

Figure 8: The decay chain of ^{238}U [11].

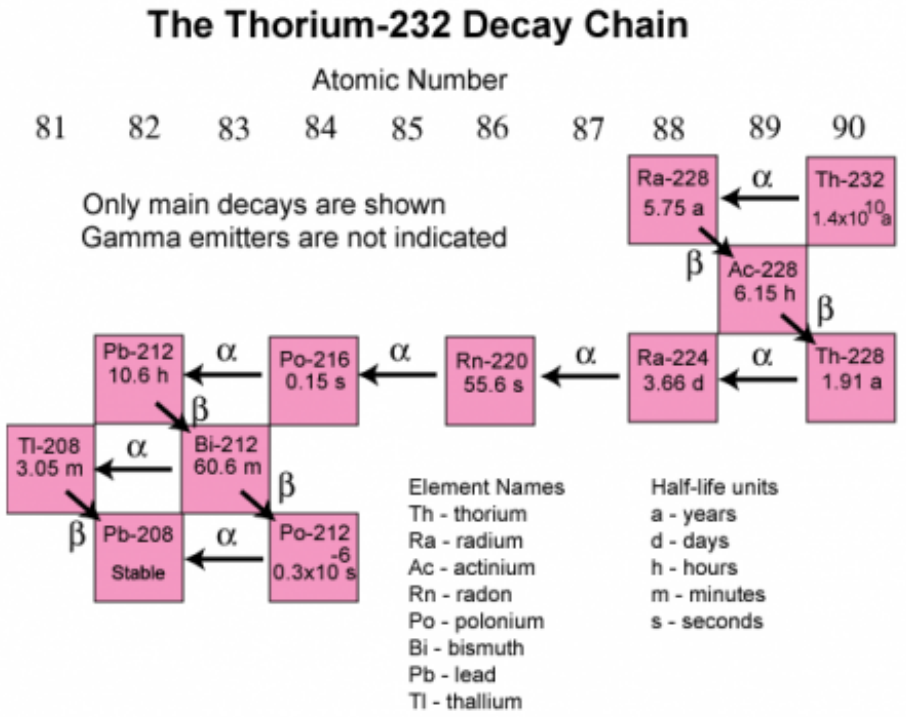

Figure 9: The decay chain of ^{232}Th [11].

2.3 Radioactive decay law and statistics

The time development of the amount of radionuclides is given by the decay law:

$$N_t = N_0 \exp -\lambda t. \tag{3}$$

Here N_t is the number of radionuclides at time t, N_0 is the number of radionuclides at $t = 0$ and λ is the decay constant of a radionuclide. An other constant worth mentioning is the half-life $T_{1/2}$. This is the time it takes for half of the radionuclides to decay and is related to the decay constant in the following way: $T_{1/2} = ln(2)/\lambda$. The last relation that should be mentioned is the rate of decay. Also known as the activity A of a source, which is given by: $A = \lambda N$.

Radioactivity is of a statistical nature and is described best by the binomial distribution, however in most situations the distribution can be approximated by the Poisson distribution:

$$P(n) = \frac{E^n}{n!} \exp{(-E)}. \tag{4}$$

Where E is the expected value of the distribution, n is the number of decays and $P(n)$ is the probability that n decays will be observed within a unit time. The Poisson approximation is only valid when $n << N$, here N is the number of radionuclides present.

The value of E is often not known, but can be approximated by taking the mean of multiple measurements. So if there are a total of m measurements each with an n amount of counts the approximation is given by:

$$E \approx \overline{n} = \frac{\sum x_i}{m}. \tag{5}$$

Here $\overline{n}$ is the average amount of counts.

To get an idea of the uncertainty in a measurement the width of the distribution can be used. The parameter describing the width is called the variance and is given by: $var = E$, if $p << 1$ where p is the probability of detection. The standard deviation is also related to the variance by the following relation: $\sigma^2 = var$.

To indicate the quality of the result one should state the confidence limits. These limits specify the degree of confidence, that the true value lies somewhere within them. The result x could be expressed as: $x \pm \sigma$. Here the confidence limits correspond to one standard deviation which implies a confidence of 68.3%, meaning that the probability of a measurement lying in the given range is 68.3%. This confidence can be increased by using multiple standard deviations as confidence limits. These limits are also often written as percentages of the measured value to make the quality of the result more clear.

When combining multiple measurements, by taking a simple mean, is in many cases not valid, since the variance of all results needs to be equal. The correct way of combining them would be with a weighted mean:

$$\overline{x} = \frac{\sum x_i w_i}{\sum w_i}. \tag{6}$$

Here w_i is given by: $w = 1/\sigma_i$ and the internal variance of the combined result is then: $var_{in} = 1/\sum w_i$. Because the internal variance could give an inaccurate result of the uncertainty a second type, called the external variance, is often also calculated:

$$var_{ex} = \frac{\sum (x_i - \overline{x})^2 w_i}{\sum w_i (m-1)}. \tag{7}$$

It is useful to be able to know when the number of counts measured is significantly above the number of background counts, For this Stapleton's decision criteria [12] can be used, it states that a count is significant if $Z > k_\alpha$. Here k_α is a factor used to set the degree of confidence and Z is given by:

$$Z = 2\frac{\sqrt{\frac{N_g+a}{t_g}} - \sqrt{\frac{N_b+a}{t_b}}}{\sqrt{\frac{1}{t_g}+\frac{1}{t_b}}}. \tag{8}$$

Where N_g is the number of gross counts, N_b is the number of background counts, t_g is the measurement time of the gross counts, t_b is the measurement time of the background counts and a is an arbitrary factor, $0 < a < 1$. Stapleton advised to set a to 0.4 if $\alpha = 0.05$, the corresponding value for k_α would then be 1.645. Here α represents the probability that a false positive could occur. In table 2 more values for α and their corresponding k_α values are listed. For equation 8 and 9 the one-tailed probability column is used, because it is about exceeding the limit on one side, namely the higher side.

An other way to determine when a count is significant, is with the critical limit L_c. If the net count is more then the L_c a count is considered valid, with a certain degree of confidence. The critical limit is given by:

$$L_c = k_\alpha \sigma_0 \tag{9}$$

Here σ_0 is the standard deviation of the background count distribution, given by: $\sigma_0 = N_b + var(N_b)$.

From equations 8 and 9 a decision level L_d can be derived. This decision level gives the minimum number of net counts needed to state that a source has been detected. The L_d can be acquired from Stapleton's decision criteria by noting that $N_g = N + N_b$, where N is the number of net counts. Substituting this into equation 8 and solving for N gives:

$$N = t_g(\frac{Z}{2}\sqrt{\frac{1}{t_g}+\frac{1}{t_b}} + \sqrt{\frac{N_b+a}{t_b}})^2 - N_b - a. \tag{10}$$

If Z is then set to $Z = k_\alpha$, equation 10 will give the L_d for Stapleton's decision criteria which is called L_ds to specify that.

From equation 9 the L_d can be directly found by realizing that $L_c = L_d$. The L_d from the critical limit will be called L_dc to be clear.

Table 2: k_α factors for particular probability intervals and the associated degrees of confidence [2].

Probability interval, α	1-tailed confidence	2-tailed confidence	k_α factor
0.1587	84.13	68.27	1.0
0.1	90.00	80.00	1.282
0.05	95.00	90.00	1.645
0.025	97.50	95.00	1.96
0.02275	97.73	95.45	2.00
0.01	99.00	98.00	2.326
0.00621	99.38	98.75	2.5
0.005	99.50	99.00	2.576
0.001 35	99.87	99.73	3.0

3 Estimating the minimal source strength detectable

For estimating the minimal source strength detectable the L_d can be used, in the section above two different formula are given to calculate this value. In this section these formula are compared to each other and one will be used for estimating the minimal source strength detectable.

In figure 10 the decision levels from both formulas are plotted against the background. It can be seen that the formula have a similar shape except that the L_{ds} seems shifted upwards by a few counts with respect to L_{dc}. This was expected, since from the analyses in the paper of Strom and Maclellan [12] it was found that the decision limit, given by L_{ds}, stayed closer to the desired false positive rate, set by the parameter α, then the decision limit given by L_{dc}. The false positive rate was higher when using L_{dc} in low count situations, therefore the decision limit should be lower.

In figure 11 the difference in the two decision levels is plotted with respect to the background. It can be seen that in the case of low background counts the difference is significant, but when more background counts are registered the difference becomes less significant and from about 100 counts could be neglected.

Because the number of background counts will frequently be below 100 counts, due to the short integration times and small detector. The detection limit that should be used is L_{ds}, since it is more accurate in this regime.

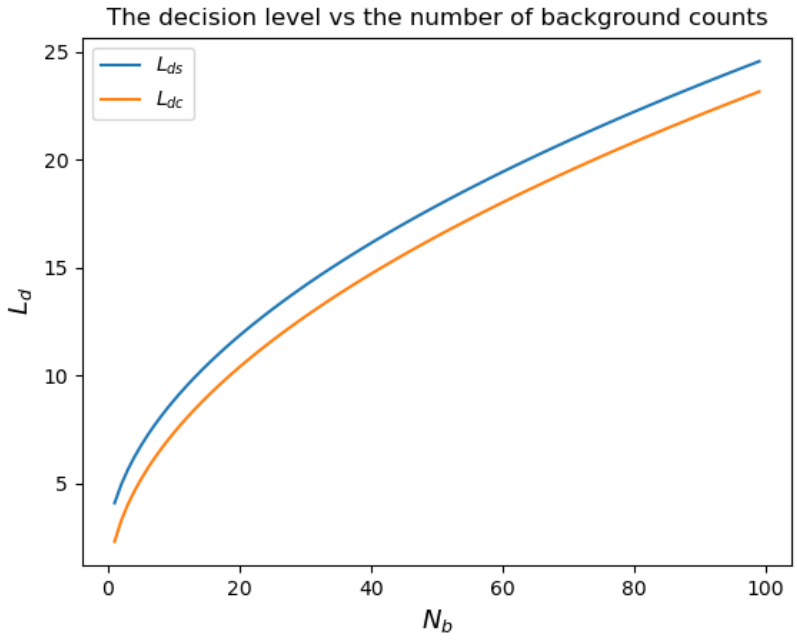

Figure 10: The decision level given by Stapleton's decision criteria L_{ds} and the critical limit L_{dc} is plotted against the background counts. for both formula the value of alpha was set to $\alpha = 0.05$ leading to $k_\alpha = 1.645$, for the L_{ds} the measuring times were set as: $t_g = t_b = 1$ s and a was set to 0.4.

To get an estimate of the background signal in the detector a monte carlo simulation of the detector positioned 80 *cm* above the ground was performed. From these simulations standard spectra for the distributed sources: ^{232}Th, ^{238}U, ^{40}K and ^{137}Cs were derived in Bq/kg . For a point source only a standard spectra of ^{137}Cs was created with the unit Bq. These standard spectra could be scaled to represent the detector response at different heights. The scaling factor for distributed sources was found with the following formula [13]:

$$F_d = \frac{E_2(h_c \mu_a \rho_a)}{E_2(h \mu_a \rho_a)}. \tag{11}$$

Here F_d is the scaling factor for distributed sources, E_2 is the exponential integral of order 2, μ_a is the energy dependent mass attenuation factor for air, ρ_a is the density of air, h_c is the height at which the standard spectra is created and h is the height at which one wants to know the standard spectra.

The scaling factor for point sources can be found with a different formula, namely [13]:

$$F_p = \frac{\exp(-d\mu_a\rho_a)}{\exp(-d_c\mu_a\rho_a)}(\frac{d_c^2}{d^2}). \tag{12}$$

Where d_c is the distance for which the standard spectrum is created and d is the distance at which one wants to know the standard spectrum.

For the specific scaling factors F_d of ^{232}Th, ^{238}U and ^{40}K the value for μ_a was kept constant and was set to their prominent energy peaks: 1.46 MeV, 1.77 MeV and 2.61 MeV respectively. For the scaling factor F_p of the ^{137}Cs point source the value of μ_a was set to 0.662 MeV.

When the standard spectra are multiplied with the appropriate scaling factor and with the data in column 3 of table 1 the background signal at different heights could be estimated.

From this background signal the L_{ds} was calculated within the energy window of the ^{137}Cs peak. In the total spectrum the peak showed predominantly in the energy range from 620 KeV to 720 KeV. Therefore this energy range was used to calculate the value of L_{ds}. For this calculation the total amount of background counts in this energy range was used as N_b, the measuring times were set equal $t_g = t_b$ and k_α was set to 1.645.

To find the strength of the point source needed to reach the L_{ds} on top of the background, the L_{ds} was divided by the amount of counts within the energy window of the standard point source spectrum from ^{137}Cs. This standard spectrum was adjusted for the distance to the detector with the factor F_p. The relation with the flight height and the minimal source strength needed to be able to detect the source found this way, is given in figure 12.

To assess which source strength could be detected in a certain field, the distance to a source on the ground D_g vs the minimal source strength needed to detect it, is plotted in figure 13a. The distance to the detector D_d was calculated with $D_d = \sqrt{D_g^2 + H^2}$, here H is the fly height. For clarification there is also a graph of the parameter D_d vs the minimal detectable source strength in figure 16a.

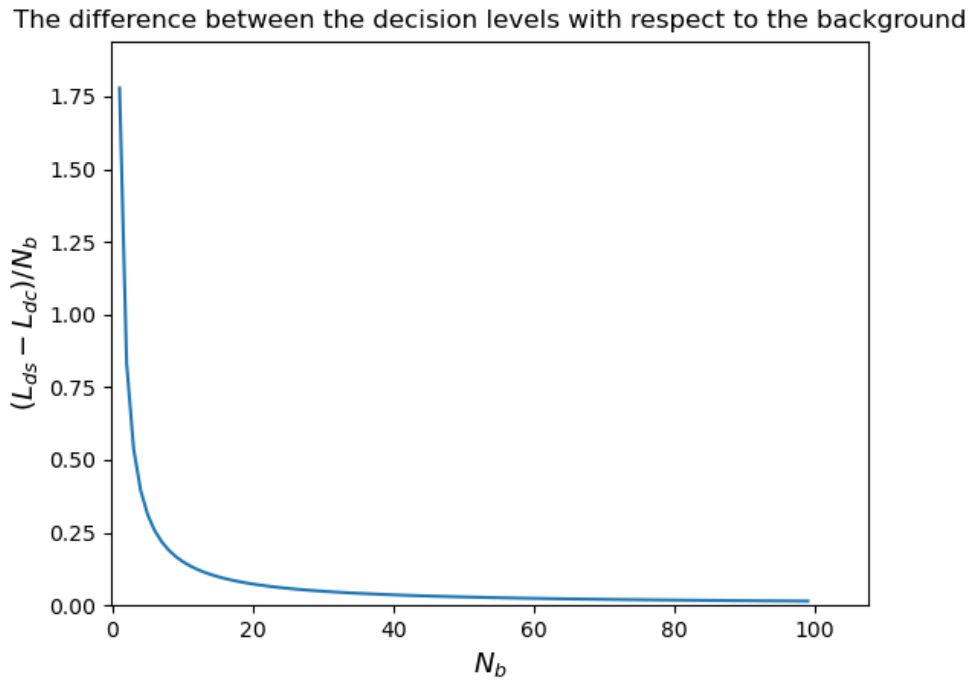

Figure 11: The difference between the decision levels with respect to the background counts is plotted. The data in figure 10 was used to create this graph.

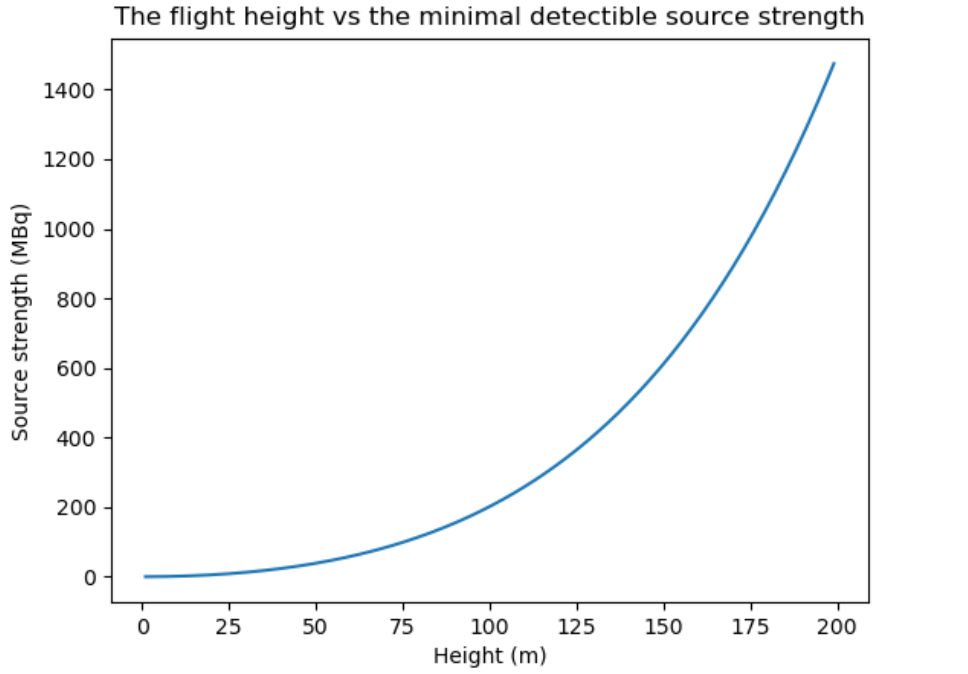

Figure 12: The minimal source strength needed to be able to detect the source is plotted against the flight height, in the case when the detector is positioned above the source. The graph is taken for an integration time of 1s.

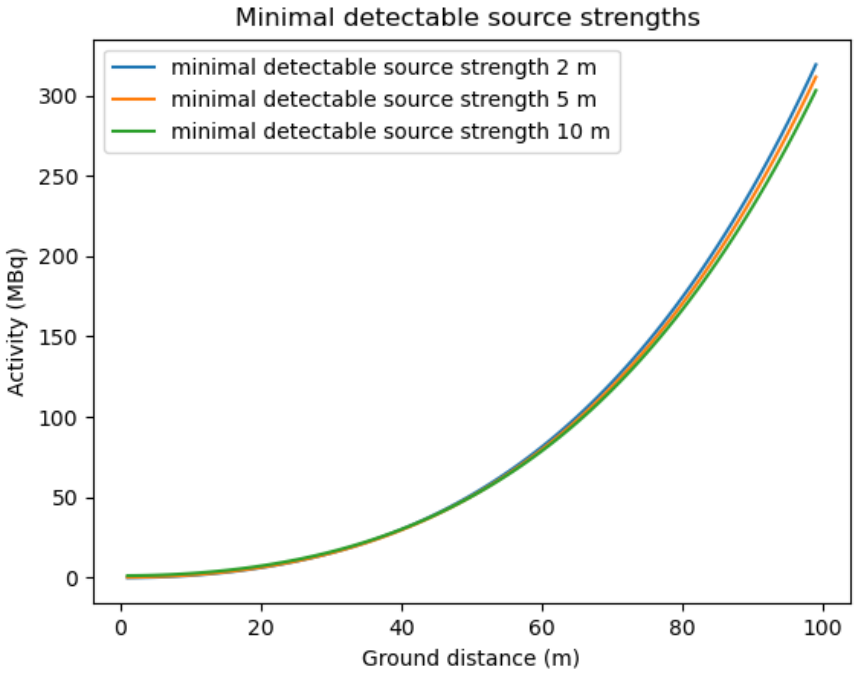

(a)

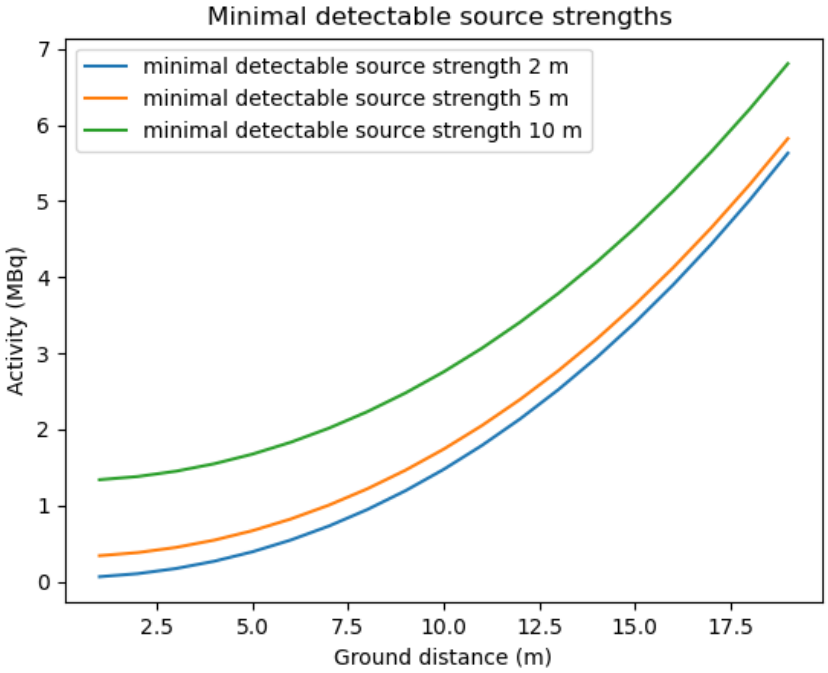

(b) The graph zoomed in on the left part.

Figure 13: (a) shows the full graph and (b) shows the graph for a distance up to 20 m. The distance to a source on the ground against the minimal detectable source strength is plotted, for the fly heights 2, 5, and 10 m. The integration time was set to 1 s.

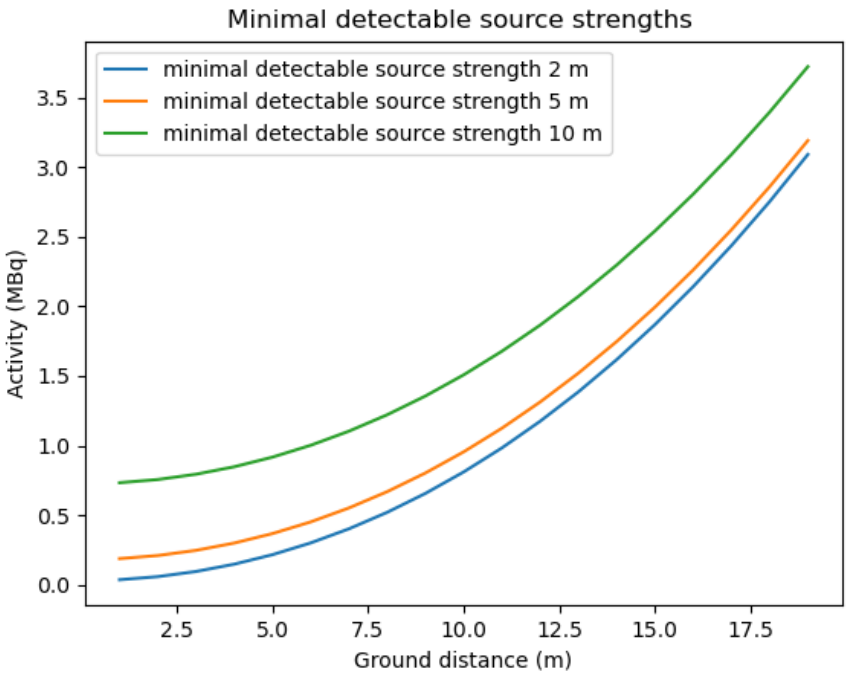

Figure 14: The distance to a source on the ground against the minimal detectable source strength, for the fly heights 2, 5, and 10 m. The integration time was set to 3 s.

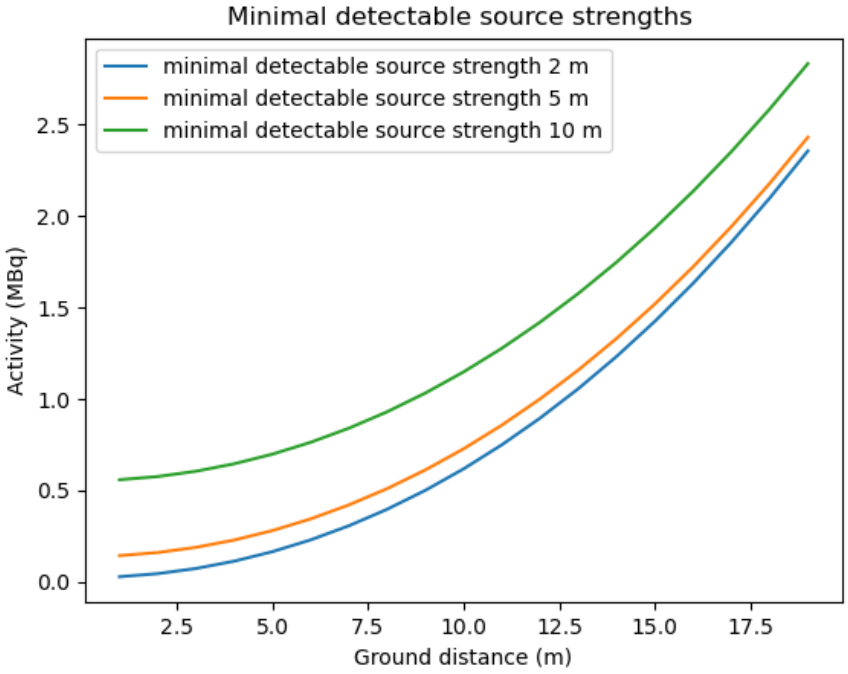

Figure 15: The distance to a source on the ground against the minimal detectable source strength, for the fly heights 2, 5, and 10 m. The integration time was set to 5 s.

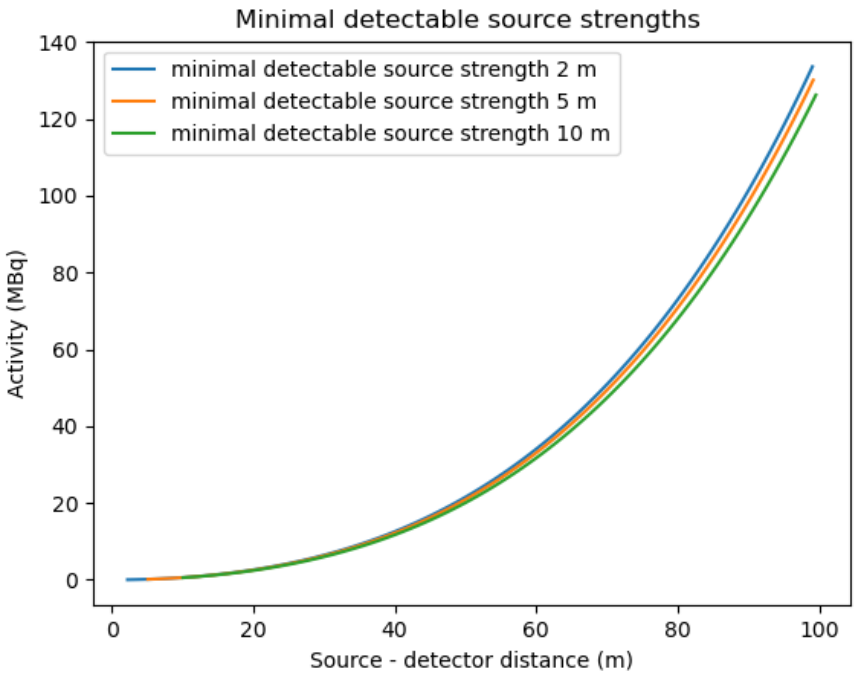

(a)

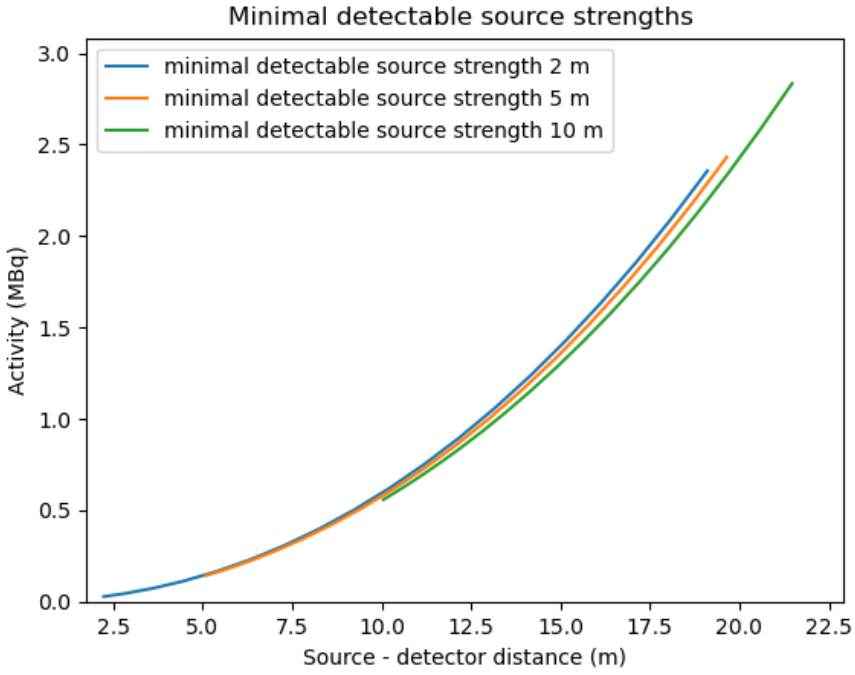

(b)

Figure 16: (a) shows the full graph and (b) shows the graph for a distance of up to 20 m. The distance of the source to the detector against the minimal detectable source strength is plotted, for the fly heights 2, 5, and 10 m. The integration time was set to 5 s.

In figure 13a it can be seen that the source strength needed, increases exponentially with the ground distance. At lower fly heights the source is easier to detect when it is close as can be seen in figure 13b. Weaker sources can also be detected if the integration time is increased to 3 s or 5 s, as shown in figure 14 and 15

An interesting feature in the graph is that the higher fly heights can detect a source that is far away easier then the lower fly heights, even though the source is further away. This is caused by the reduced background at higher altitudes. Thanks to this there are less counts needed to detect the source, which can be useful if the distance is dominated by the ground distance $D_g >> H$. It is only useful in this limit because then the increase in distance due to fly height is negligible and the reduced background creates better detection circumstances.

To be able to predict at what kind of distances the sources used in the experiments could be detected, the values from the model should be scaled to accommodate for the different detector properties. This can be accomplished by scaling the results with respect to the detector volume, used in the calculations of this section. The CsI crystal of the detector used in the calculations above has a size of 2000 ml. While the detectors used in the experiment have a 350 ml CsI crystal or a 12.8 ml CeBr3 crystal. Therefore a conversion factor of $2000/350 \approx 5.71$ is used for the 350 ml detector and a conversion factor of $2000/12.8 \approx 156$ is used for the 12.8 ml detector. Via this factor, it is assumed that the detection probability scales linear with the volume of the crystal. This is a very simplified model, because a lot of other factors are not considered. These factors include the direction of the gamma rays, the surface area of the crystal, the kind of crystal and the full energy peak efficiency. The best way to encompass all these variables properly is by doing a Monte Carlo simulation for each detector, but for the purpose in this report the approximation is justified, since it is only meant to give an estimation of what to expect from the experiments.

The sources used in the experiment are a 1.3 MBq ^{137}Cs source and a 0.7 MBq ^{22}Na source. So for these sources the detectable distances is calculated. This calculation is performed by multiplying the minimal source strength needed, with the conversion factor of the detector. Then the height where the minimal source strength detectable equals the source strength of the experiment, is selected as maximal detectable distance.

From the small 12.8 ml CeBr3 detector it is expected that a ^{137}Cs source with a strength of 1.3 MBq is detectable up to a height of 1.7 m above the source for a 20 s integration time and 0.8 m for a 1 s integration time. If the detector would be kept at a constant height of 5 cm from the ground, the source should be visible up to 2.2 m for a 60 s integration time and up to 0.6 m for a 1 s integration time. The background counts are expected to drop at higher altitudes leading ta a decrease in the decision level.

The detector with a 350 ml CsI crystal should detect the 0.7994 MBq ^{22}Na source up to a height of 7 m when flying above it and integrating over a 5 s time interval. This was estimated by converting the ^{22}Na source to a ^{137}Cs source, such that the number of 511 keV annihilation photons from ^{22}Na equals the number of 662 keV photons from ^{137}Cs. This was achieved with the use of the following equation: $2 * P_{Na} * S_{Na}/P_{Cs} = S_{Cs}$. Here P_{Na} represents the branch probability for β^+ decay of ^{22}Na, the P_{Cs} is the probability that a 137cs decay produces a 662 keV gamma ray , the 2 is for the number of annihilation photons resulting from the beta plus decay, the S_{Na} and S_{Cs} are the strength of the ^{22}Na and ^{137}Cs source. When substituting in the numbers one gets: $0.90 * 0.7994 * 2/0.85 = 1.7$ MBq, the branching probabilities were found in source [14].

4 Search algorithms[3]

When searching for an radioactive source with a drone there are two known parameters, the first being: the position of the drone, the second being: the radiation detected at that position. To be able to calculate the distance to the source one also needs to know the strength of the source and what kind of source it is. If this information is not available the source could be located by searching for the spot with the highest activity. Since searching for the spot with the highest activity is the most general case the focus will be on these kind of source localization algorithms. Each of the different algorithms explained will be based on the same assumptions the first assumption being: the interested area is a rectangle that is P meters wide and O meters long. The second assumption is: the drone is always at a constant height and therefore the problem can be reduced from a 3-dimensional to a 2-dimensional problem.

The first algorithm that will be discussed is the traversal search algorithm. the flight path of this algorithm is shown in figure 17a. For this search tactic the short side of the rectangle is divided into smaller sections of length N. Then the drone starts at a corner of the rectangle and flies along the longest side until it reaches the edge. Now it flies a distance of N meters along the shorter side after which it flies back to the other side in a straight line. This is repeated until the drone reaches the other long side of the rectangle. The spot on the map with the highest activity is then set as the location of the source. This tactic is the slowest, but also the most simple, because the flight path does not change with the source location.

The second search algorithm is shown in figure 17b and is called the Binary search algorithm. To find the source the drone will fly along the top boundary, the bottom boundary and the bisector of the top and bottom boundary. Then it will calculate the average activity measured over the three paths and discard the path with the lowest average activity. The two remaining paths will be defined as the new field boundaries. This procedure is also followed with the left and right boundary, until a predefined minimal distance between the boundaries is reached. There will then be a smaller area that is likely to contain the source. The search time with this algorithm is reduced significantly, because it discards half of the area each time. However one needs to be able to detect the source at the boundary or middle of the rectangle. Therefore the search algorithm is only suited for search areas where the source can be detected within 1/4 of the area.

The third search algorithm is called: Successive approximation, see figure 17c. The source is located by flying over the long boundary of the search area and selecting the spot with the highest activity. Then the drone flies perpendicular to the previous path into the search area until it reaches the other boundary. After this flight the point with the highest activity is selected as the source location. This theory relies on the result that any chord of a circle can be evenly divided by a perpendicular line that will go through the center of the circle. For this algorithm to work an even bigger constraint on the search area needs to hold. There should be an significant change in activity detected along the boundary, requiring an even stronger source then for the Binary algorithm.

A variation on the traversal search algorithm can be made by dividing the area into squares of N by N meters. and measuring at every intersection point by hovering the drone there. However because the drone would need to brake and accelerate more often this is less efficient, therefore less measurement points can be made in the same time. Increasing the average distance of the measurements to the source, therefore a continuous flight path was chosen.

[3]The three search algorithms discussed here were found in reference [15].

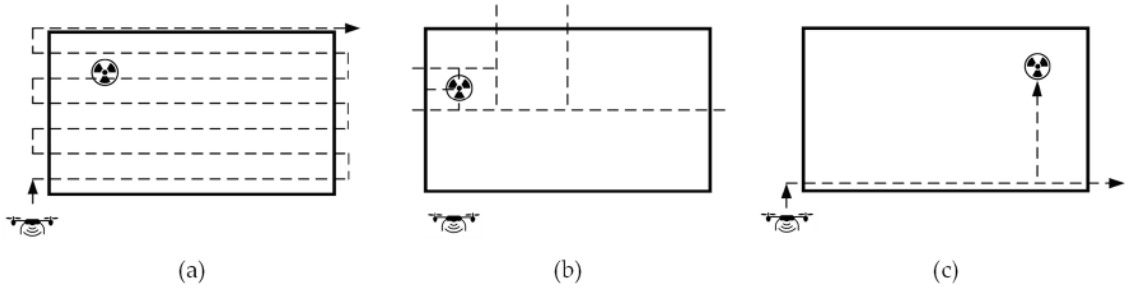

Figure 17: (a) shows the traversal search algorithm, (b) shows the binary search algorithm and (c) shows the successive approximation search algorithm [15].

5 Experimental methods

To find how well the predicted values for background radiation and detection distances correspond with the real world a set of measurements were taken with a small detector mounted on a drone, see figure 18. The detector used has a CeBr3 crystal of 12.8 ml and the drone was a customized DJI phantom 4. The gimbal camera of the drone was removed to save weight and the detector with a Raspberry Pi 3b+ and a Ublox NEO-m8n GPS was mounted on the drone. The detector, raspberry pie and GPS were powered via the drones internal electronics.

Figure 18: The customized DJI phantom 4 with the 12.8 ml CeBr3 crystal detector.

Part of the measurements were also done with a bigger drone and detector. The bigger drone was a DJI Matrice 600 pro with a detector mounted on the underside. The detector was a Medusa Radiometrics MS-350, 350ml CsI scintilattion detector with an integrated GPS [16]. See figure 19 for the full setup.

Figure 19: The DJI Matrice 600 pro setup with the MS350 mounted underneath it.

Three different sources were used during the experiments namely:

- ^{137}Cs, 50 μCi on 3-2005
- ^{22}Na, 1.040 MBq on 15-6-2019
- Uranium tailings, 19 kBq of ^{238}U on 11-11-1999

The ^{137}Cs and ^{22}Na had a strength of about 1.3 MBq and 0.7994 MBq respectively, at the day of the experiment, 10-6-2020. These strengths were calculated with the use of equation 3 and the half life of the radionuclides, 11018.3 $\pm$ 9.5 d for ^{137}Cs and 950.97 $\pm$ 0.15 d for ^{22}Na [17]. For the case of the uranium tailings it was assumed that the decay chain was in equilibrium and that all decay products thus have the same activity as ^{238}U, what leads to an activity of $14 * 19 = 0.27MBq$, where 14 is the amount of decay products in the decay chain of ^{238}U. The decay of the uranium tailings was neglected, since the half life is $4.5 * 10^9$ y [18], so only $4.7 * 10^{-7}$% of the half live has passed on the date of measuring.

The measurements were taken in 4 different setups, the first setup was focused on finding the relation between source distance and detect ability with a constant background. The second setup

was created to find the relation between the source distance and detect ability with a varying background. The third setup was made to test the ability of the drone to locate a source when flying in a grid pattern and the fourth setup was created to test how the fly speed would effect the accuracy in locating the source.

The first setup was created by placing the source and the drone on the ground. Then the distance between the drone and the source was varied from 50 cm to 350 cm, with steps of 50 cm. The integration time of the detector was set to 1 s and left to measure for at least 80 s in total. A background measurement was also made by placing the drone at the middle of the measurement path and removing the source. Because the detector has a constant height from the ground the background during this experiment was assumed to be constant.

The second setup consisted of two parts in part 1 the customized Phantom 4 was used and in part 2 the Matrice 600 pro was used. In both cases the drones were hovering above the source at different heights. For part 1 the ^{137}Cs source was put placed on the ground and a measuring tape was put on top of it, to make sure it would not blow away. The Phantom 4 would hover at heights ranging from 50 cm to 300 cm with 50 cm intervals. The integration time of the detector was set to 1 s and the drone would maintain each height for at least 38 s. Background measurements were also taken at each height. In part 2 the ^{22}Na source was used, this time the source was placed on the ground in a potato field. The Matrice 600 pro would hover above the source for at least 20 s, in the range of 1 m until 12 m with 1 m intervals. There was only one background measurement made at a height of 6 m.

In the third setup, a grid pattern was flown at two different heights, namely: 50 cm and 100 cm. The grid was flown manually by following the pattern on the floor, see figure 20. The sources used were again secured in place with a measuring tape and the integration time of the detector was set to 1 s. For a part of this experiment all three sources would be placed together to increase the count rate. This will be referred to as multiple sources.

The last setup consisted of flying past the source at different speeds, with a height of 50 cm. This was also done manually and the integration time was again set to 1 s. During this setup only the multiple sources configuration was used.

Figure 20: The test location where the measurements with the customized DJI phantom 4 were taken.

6 Results

6.1 Setup 1

In figure 21 the result of the first measurement is shown for a distance of 350 cm. In the graph a peak around 660 keV can be seen and the decisions level was reached for both spectra.

For the calculations of the decision level equation 10 was used with $Z = k_\alpha = 1.645$, N_b as the total background counts over the whole spectrum or in the peak energy window (620 keV to 700 keV), t_b as the background integration time and t_g was set to the integration time, at which one wants to know the decision level. For this experiment it would be 60 s and 1 s respectively, to the resulting value are the number of background counts, added to get the number of gross counts needed for detection N_g. For the 60 s integration time this would result in $N_g = 20.2$ for the peak area counts and for the 1 s integration time it would result in $N_g = 1.27$ counts in the peak area.

In figure 22 the total counts per second distribution of the background, the detected spectra, according to the peak area decision level, and the not detected spectra, according to the peak area decision level, are shown. In table 3 the results of all measurement distances are shown, it can be seen that the percentage detected spectra was higher when the total counts were used.

Table 3: Here the percentage spectra where the source is detected with 95% certainty is shown. This is based on the amount of spectra where the counts in the peak area or the total counts were bigger then the decision level for peak area counts or total counts. The last row includes spectra that passed either the peak area decision level or the total counts decision level.

	Source distance (dm)						
	5.0	**10**	**15**	**20**	**25**	**30**	**35**
Percentage detected when only using peak area	100	94	45	10	3	2	0
Percentage detected when only using total counts	100	99	70	23	15	7	5
Percentage detected when using both total counts and peak area	100	99	80	28	16	9	5

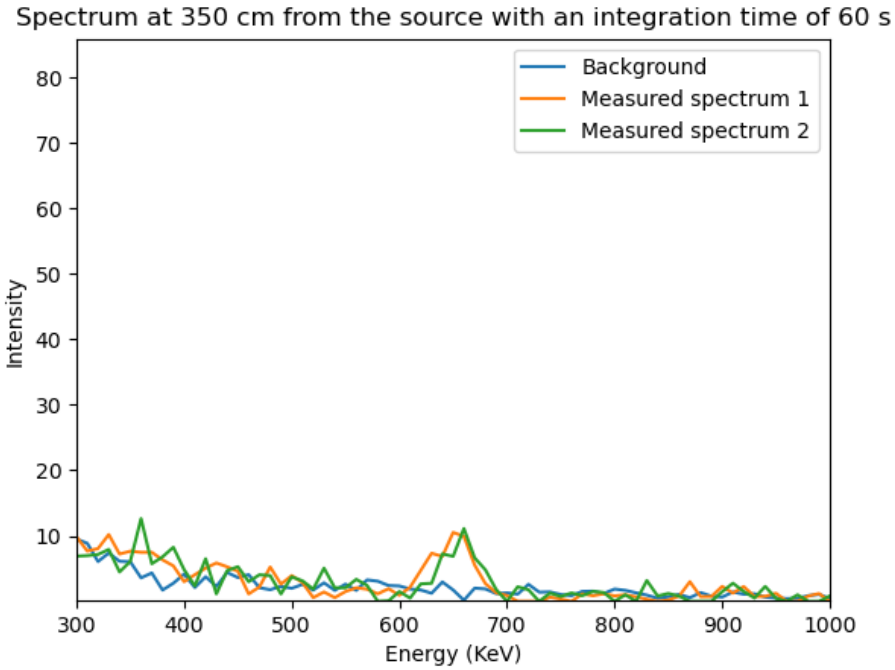

Figure 21: The spectrum resulting from a measurement at a distance of 350 cm and an integration time of 60 s. The background shown was measured with an integration time of 209 s.

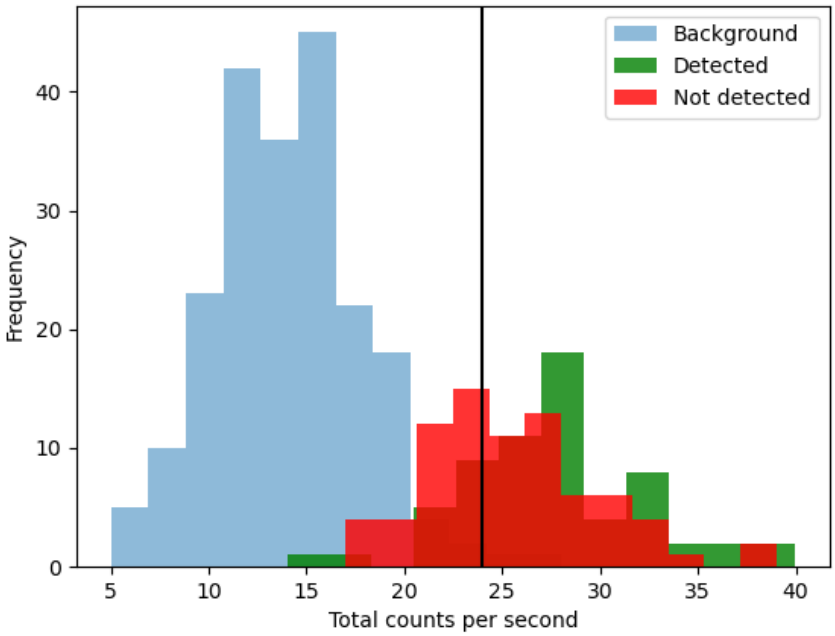

Figure 22: A histogram resulting from the measurement at a distance of 150 cm. The Background histogram shows the total count distribution of the background. The detected histogram shows the total counts distribution of the measurements that are above the gross count decision limit in the energy window from 620 keV up to 700 keV. The not detected histogram shows the total counts distribution of the measurements that are below or equel to the gross count decision limit in the energy window from 620 keV up to 700 keV. The vertical line is the decision level based on the whole spectrum.

6.2 setup 2

6.2.1 part 1

In figure 24 a peak around 660 keV can be seen for all three measurements. They are also all above the gross count peak decision level of 7.72 counts, resulting from the background measurement at a height of 30 dm. In figure 23 the mean total background counts is plotted against the fly height. In the model a correction for the concrete ground was applied by changing the concentrations of the natural occurring isotopes ^{40}K, ^{238}U and ^{232}Th to 410 bq/kg, 40bq/kg and 25 bq/kg respectively [19]. It can be seen that the theory predicts a lower number of counts and a decreasing trend, while the measurements show an increasing trend. In table 4 the results of the background measurements are shown, together with their standard deviation and integration time.

Table 4: here the integration time of the background measurement, the mean total count rate per second $\bar{x}$ and the standard deviation σ of the background counts are shown.

	Fly height (dm)						
	0	**5.0**	**10**	**15**	**20**	**25**	**30**
Integration time (s)	209	223	93	96	88	80	53
$\bar{x}$	13.8	14.2	14.0	15.1	15.1	14.8	15.0
σ	3.9	3.8	3.6	3.5	3.8	3.7	3.6

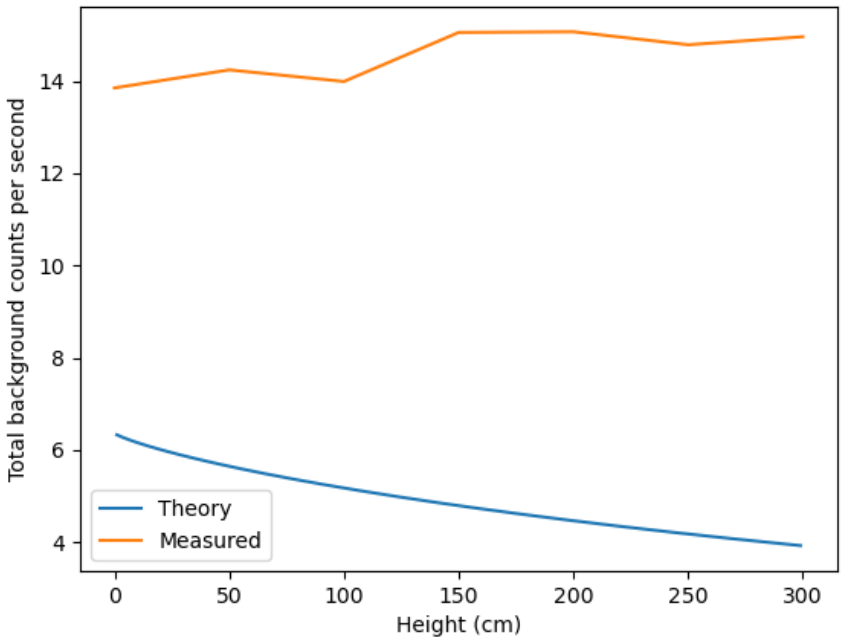

Figure 23: The mean total background counts per second vs the fly height is plotted here, for both the theory and the measurements.

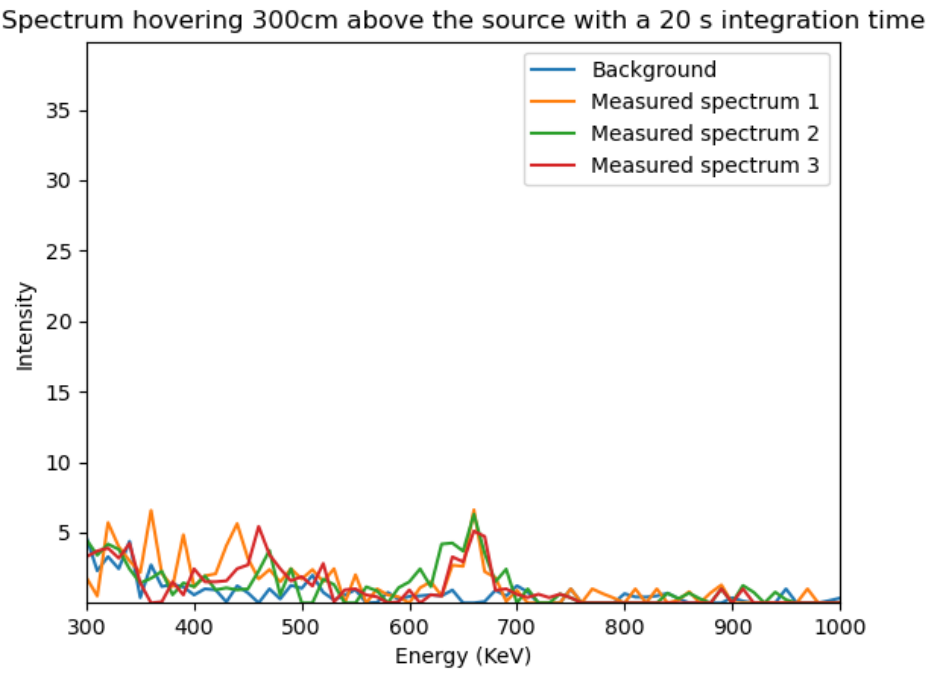

Figure 24: The measured spectra resulting from hovering 300 cm above the source, with an integration time of 20s.

6.2.2 part 2

The figures 25, 26 and 27 show the measured spectra from the source at different heights. The background in the figures is the same, since only one at 6 m was recorded. In figure 25 two peaks from the ^{22}Na source can be seen, one at 511 keV and one at 1274 keV. The next figure, figure 26, which displays the spectrum at an height of 6 m also shows a clear peak at 511 keV. However the 1274 keV peak is not as prominent. Figure 27 presents the spectrum measured at 12 m. Here the 1274 keV peak can not be seen anymore and and the 511 keV peak does only stand out in measurement 1.

The gross count decision level for this part was only calculated at a height of 6 m with 17.9 background counts in the energy interval of 450 keV until 550 keV. It was found to be $N_g = 25.1$ counts for the same energy window, this limit was reached for 100% of the measurements until 10 m. At 11 and 12 m only the first measurement reached the limit.

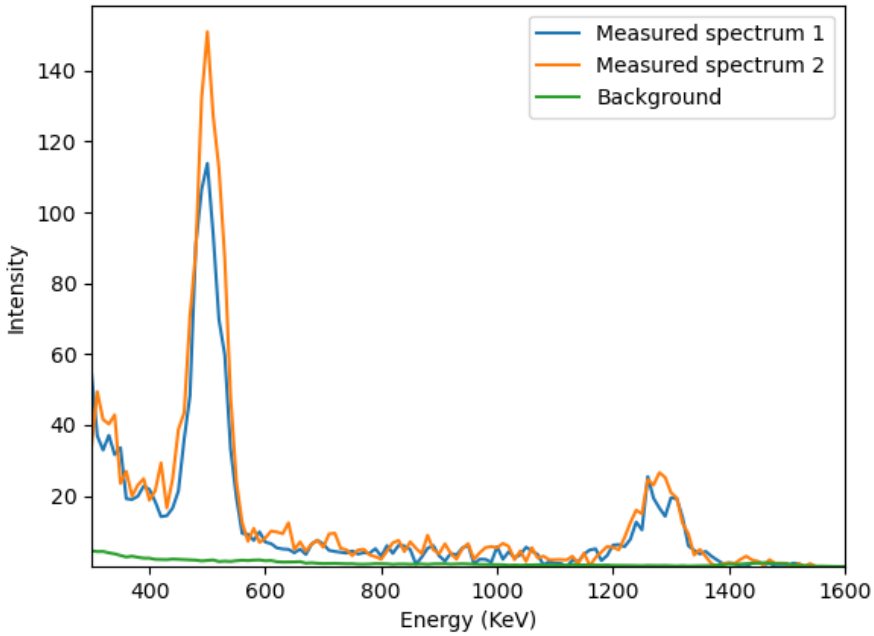

Figure 25: The measured spectra at an height of 1 m above the ^{22}Na source, each spectra has an integration time of 5 s. The background shown was measured at an height of 6 m.

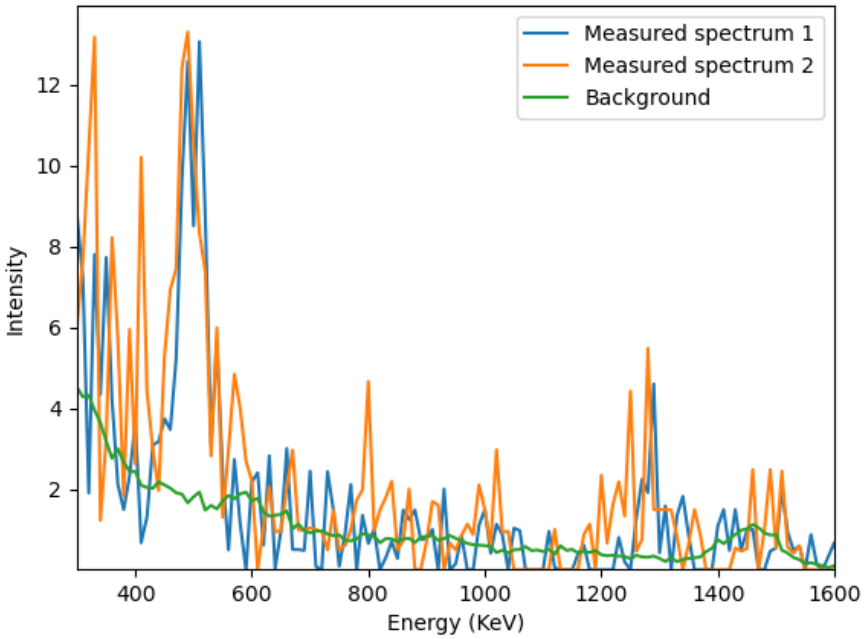

Figure 26: The measured spectra at an height of 6 m above the ^{22}Na source, each spectra has an integration time of 5 s.

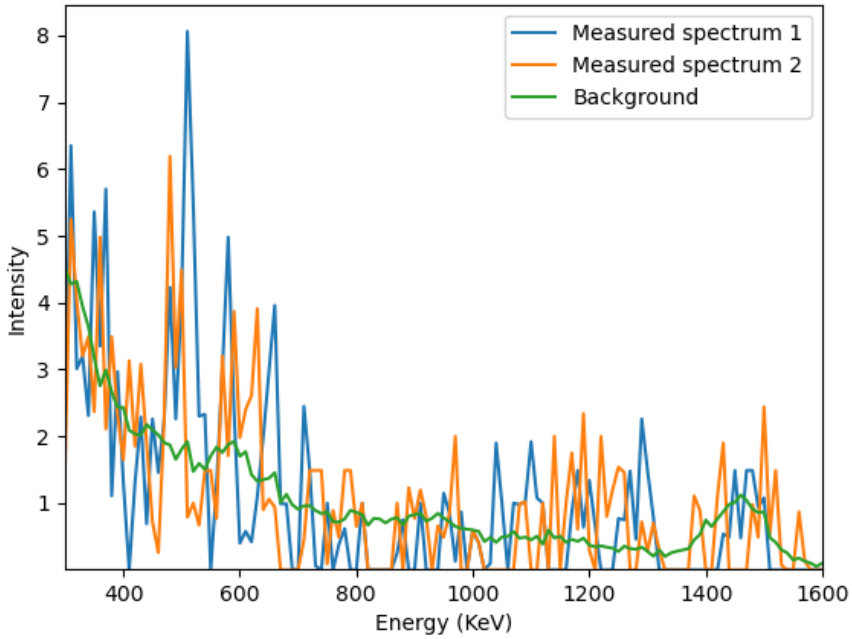

Figure 27: The measured spectra at an height of 12 m above the ^{22}Na source, each spectra has an integration time of 5 s. The background shown was measured at an height of 6 m.

6.3 setup 3

In total the traversal search flight was conducted four times. The results of these flights can be seen from figure 29 to 32. In the first flight, shown in figure 29, the GPS data from the drone and the detector correspond well, but the yellow dot indicating a high count rate is still about 4 m from the actual source location, as shown in figure 28. In the other flights the GPS data from the drone and the detector do not overlap.

In all the figures except for figure 31 there is a clear yellow spot indicating a high count rate and thus the presence of a source. In table 5 the coordinates of the yellow dot and the distance from the source is shown.

	Yellow dot coordinates		Distance (m)
	Longitude	Latitude	
Flight 1	53.249945	6.525193	4
Flight 2	53.249920	6.525243	6
Flight 4	53.249955	6.525236	2

Table 5: The coordinates of the yellow dot is the place with the highest measured count rate. The distance is the length of a straight line from the yellow dot to the source location, where the source location is at a longitude of 53.24997 and a latitude of 6.52523.

Figure 28: The path of flight 2 shown on top of a satellite image. The green marker indicates the starting point, the red marker indicates the end the blue marker indicates the source location and the yellow marker indicates the location with the highest measured count rate.

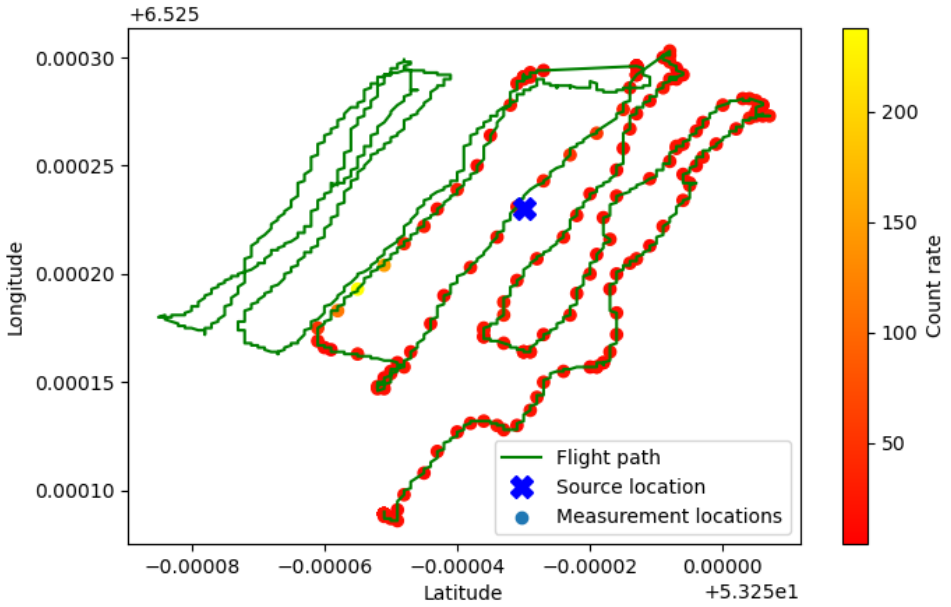

Figure 29: Flight 1 is flown at a constant height of 0.5 m and with a ^{137}Cs source located at the blue cross. The integration time of the detector was set to 1 s.

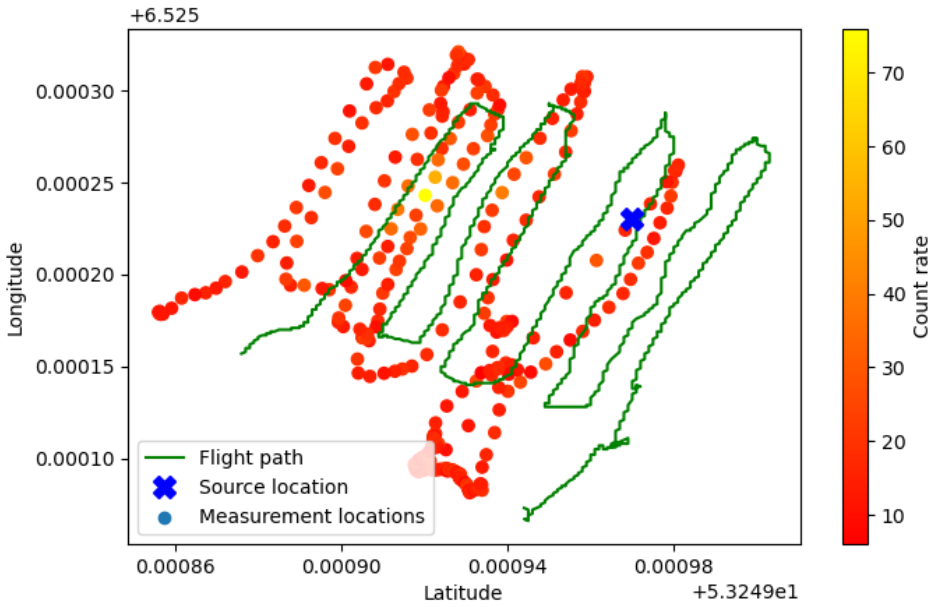

Figure 30: Flight 2 is flown at a constant height of 1 m and with a ^{137}Cs source located at the blue cross. The integration time of the detector was set to 1 s.

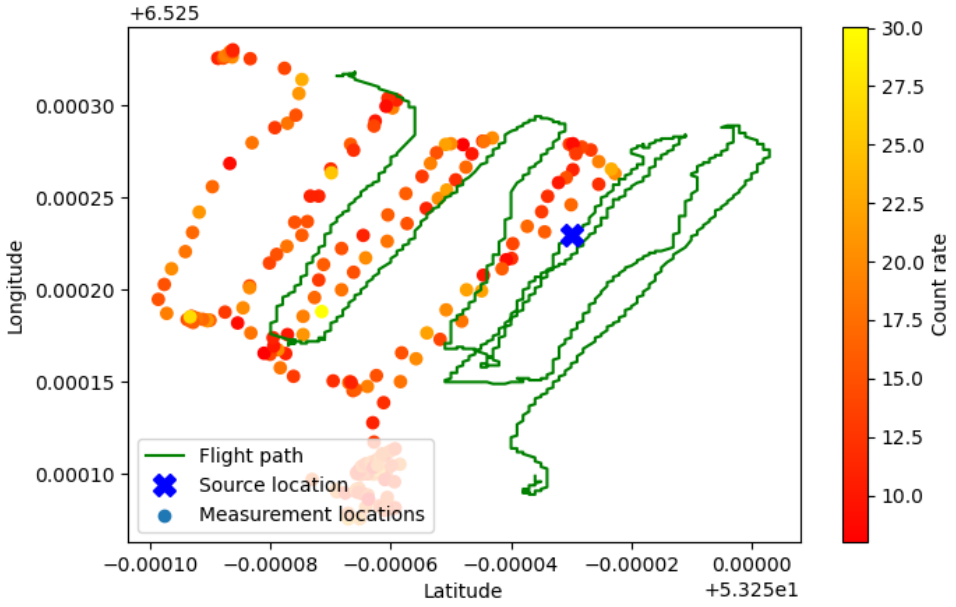

Figure 31: Flight 3 is flown at a constant height of 0.5 m and with a Wismut sand source located at the blue cross. The integration time of the detector was set to 1 s.

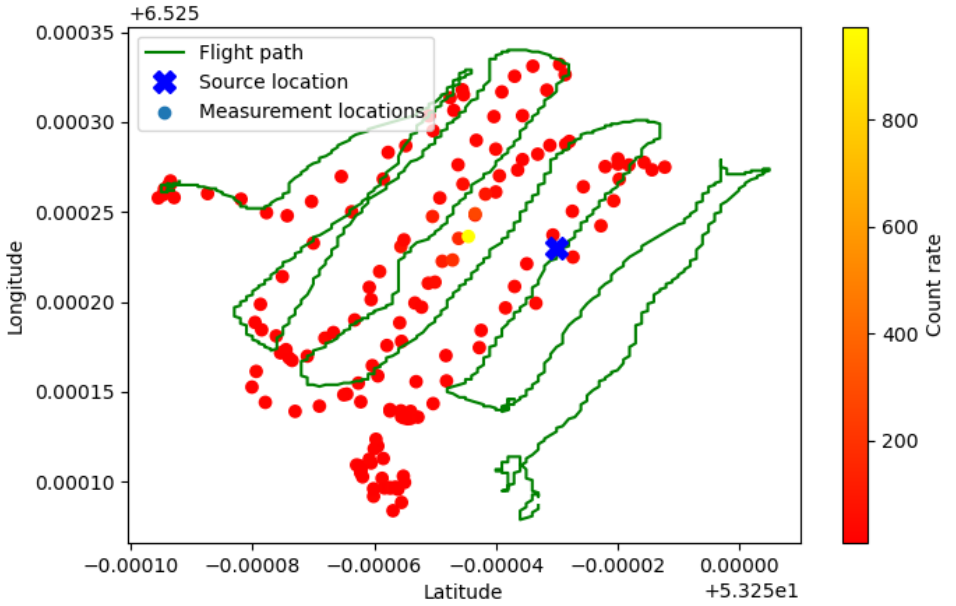

Figure 32: Flight 4 is flown at a constant height of 0.5 m and with multiple sources located at the blue cross. The integration time of the detector was set to 1 s.

6.4 Setup 4

Two flyby's were conducted at approximately 0.39 m/s and 1.3 m/s. These are shown in figure 33 and 34, it can be seen that the GPS values of the drone and the detector do not align for both flights, but there is a clear spot of high count rates in both flights indicating the presence of a source.

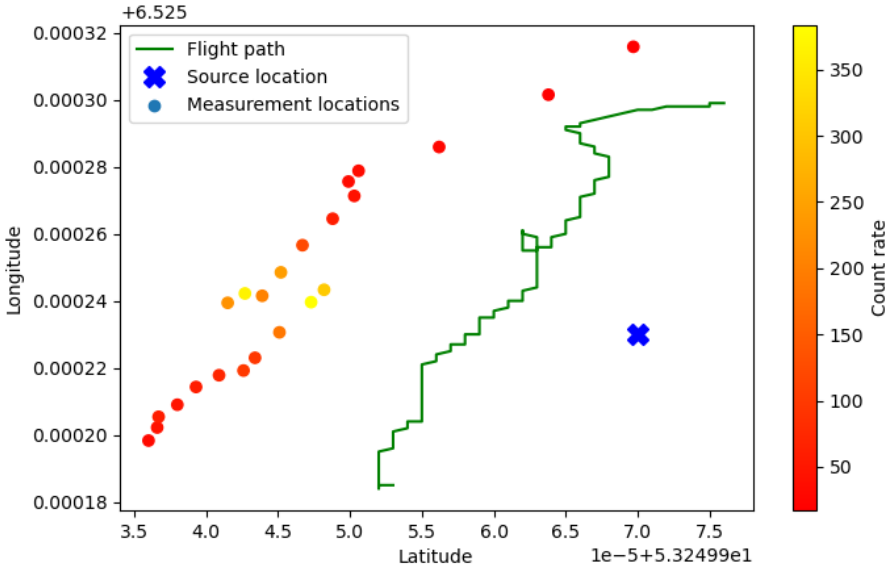

Figure 33: A fly by at a speed of approximately 0.39 m/s while flying 0.5 m high. At the blue cross multiple sources were placed. The integration time of the detector was set to 1 s.

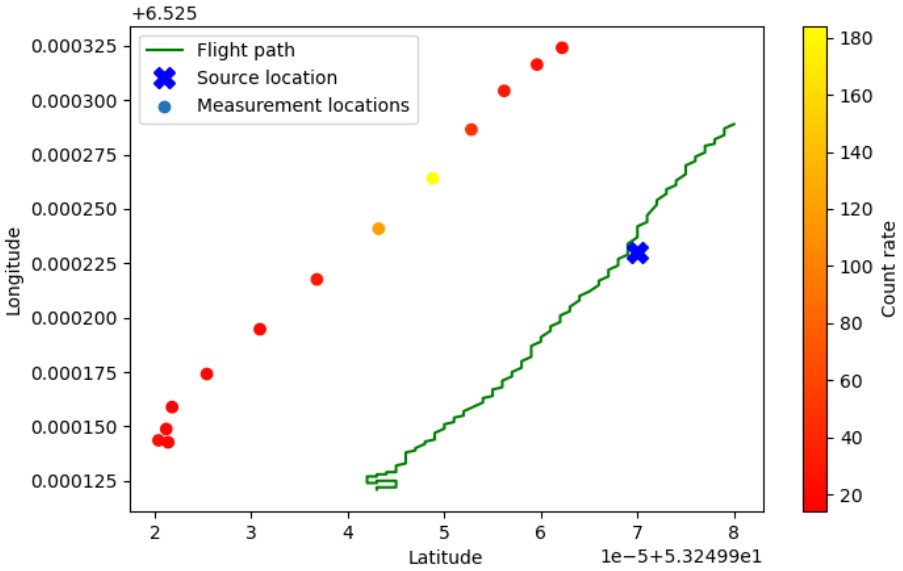

Figure 34: A fly by at a speed of approximately 1.3 m/s while flying 0.5 m high. At the blue cross multiple sources were placed. The integration time of the detector was set to 1 s.

7 Discussion

In the results of the experiments it was found that the background differs from the estimated value at both test locations. When the background of the test location is higher then predicted the source is more difficult to detect, when the background is lower then predicted the source is more easily detected. At the test location for the Phantom 4 the total background counts were about 260% higher then predicted, while at the test location for the Matrice the background counts were 166% lower then estimated. This difference in background counts is partly caused by the different ground materials at the test locations. For the Phantom 4 test location this was concrete, which has a higher natural radioactivity then soil [19]. For the test location of the Matrice this was soil with potato plants grown on it, these plants block some of the radiation from the soil. The soil could also have a lower amount of natural radiation then the typical values in table 1, which are used in the model. An other cause for the difference in background counts is the scaling factor used to take the different detector sizes into account. This factor does not correct properly for detector property differences, such as crystal type and peak to Compton ratio and is seen as the main source of error, because with correction for the concrete background the difference in total count rate was still 220%.

In all the measurements the source was detected up to greater distances then predicted by the model. In the first setup the model predicted a detectable distance of 220 cm for a 60 s integration time while the source could still be detected at 350 cm with a 60 s integration time, as shown in figure 21. In the second setup the model predicted a detectable distance of 150 cm when hovering above the source, with an integration time of 20 s. While in the results it is shown in figure 24, that the source was still detectable at 300 cm with an integration time of 20 s. This is also seen for the big detector at an predicted distance of 7.0 m, but an detected distance of 10 in 100% of the cases and up to 12 m 50% of the measurements, both measurements have a statistical accuracy of 95%. All this data shows that the model underestimates the distances to which the source could be detected between 30% and 50%. A part of the underestimation for the detectable distance of the MS350 is caused by the background being lower at the test location, this improves the result by 5%. However the estimation for the detector under the Phantom 4 gets worse when the background of the test location is used, since it is higher. Therefore it is concluded that the main cause of the error is the scaling factor.

It was found that the detection change of the source was the highest when a combination of peak area counts and total counts was used, as can be seen in table 3. This can be explained by figure 22, where it can be seen that part of the measurements which did not reach the decision level for the peak area counts do reach the decision level for total counts and vice versa. What can also be seen is that the source is more often detected when the total counts of the spectrum are analyzed, this is seen because the Compton's are now also taken into account. It is expected that this effect is more pronounced in smaller detectors due to their peak to Compton ratio being lower.

A decline in background counts was expected when the height of the drone would increase. However this was not seen in the measurements as shown in figure 23, here the number of background counts seems to increase with fly height. From a Welsh's t-test on the data for a height of 0 dm and 30 dm, a probability of 5.2% was found for the two-tailed case, meaning that there is a probability of 2.6% that the observed mean counts at 30 dm would be observed with the data from 0 dm. This value is not deemed low enough to conclude that the background actually is increasing with fly height, because more evidence is needed to disprove equation 11. What this does show is that the model creates an incomplete picture of the background by not including statistical variations.

It was found that a source of 1.3 MBq can be detected with a 12.8 ml CeBr3 crystal detector, as shown in the figures 29, 30 and 32. Here a clear peak in count rate is observed, at the location of the yellow dot. However in figure 31 no source was detected, since there is no high count rate spot. This is caused by the used source, uranium tailings, being to weak to detect.

The apparent location of the source as indicated by the location of the yellow dots, was 2 to 6 m from the actual source location. This error in source location is caused by the error in GPS location, which has an horizontal error of less then 1.9 m 95% of the time [20]. This error does suggest that the source should be within a circle of about 4 m around the source 95% of the cases. This does correspond well with the location error in flight 1 and 4, for flight 2 a bigger error of 6 m was found and it is assumed that this is an exceptional high error that occurs in less then 5% of the cases. It is thought that the error in source location would decrease if the count rate is synchronized with the GPS data of the Phantom 4, since the path according to the drone GPS corresponds better with the flown path and since DJI claims a lower error of 1.5 m [21]. The synchronization of the data was not performed because there was no time for it.

The first flight in figure 29 stands out because the drone GPS data and the detector GPS data do correspond well, suggesting that the error in the location of the count rate was low. However the error in source location is still high. The reason for the overlapping of the GPS location and the source offset could be a constant and equal error in both GPS systems. It is not attributed to a delay between the GPS signal and the count rate data, because in figure 33 and 34 there seems to be no delay between the GPS and the count rate. Part of the data for this flight was left out because all data would be distorted when it was added. The cause of the distortion could be related to the battery swap that was performed half way the first flight.

The last setup was created to find the impact of the speed of the drone on the location accuracy and the detector sensitivity. From the figures 33 and 34 it becomes clear that the density of points is lower when flying faster and thus the accuracy should be less. But this is not reflected well in the results, as can be seen in figure 33 of the slow flight. It has two, approximately equal, high count rate points with a lower one in the middle. This inaccuracy caused by the error of the GPS, makes that the slower flight is not clearly more accurate.

In the slow and fast flight there is also a clear difference in maximum count rate. This is partially caused by the difference in source distance from the flight path and the difference in flight height. For the slow flight the flight height was 3 dm while it was 5 dm for the fast flight, creating a difference of 2 dm in favor of the count rate for the slow flight. The difference in path to source distance is about 2 m for the slow flight and about 0 m for the fast flight, creating a difference of 2 m in favor of the count rate for the fast flight. Yet the fast flight still has a lower maximum count rate at 184 counts, with respect to 384 counts for the slow flight. This means that for detecting a lower strength source flight speed is of great influence.

8 Conclusion

A theoretical model for source detect ability at various distances was created and experiments with a 12.8 ml CeBr3 detector mounted under a DJI Phantom 4 as well as a 350 ml CsI detector mounted under a DJI Matrice 600 pro were performed. It was concluded that detecting a 1.3 MBq source is possible, as well as locating it, although a better positioning system is needed if an accuracy in the order of magnitude of centimeter is required. It was also found that the sensitivity of the detector decreases when the fly speed increases and that a combination of count rate and peak area counts give the best change for detecting a source. In the theoretical model the detectable distance is under estimated and the attenuation of the background signal paints a to idealized picture of the measured background at different heights, by not including statistical uncertainties.

Further research should focus on improving the location error by, for example, using an RTK gps. An other option for improvement is the search efficiency of the drone, this could be done with an other search algorithm. Yet an other focus point should on optimal integration times for sensitivity. The model should be improved by including statistical uncertainties in the predictions, the influence of fly speed and the scaling factor should be improved, by incorporating the kind of crystal used, for example.

References

[1] Terry Macalister and Richard Halpin. Radioactive materials lost in more than 30 incidents over past decade. *The guardian*, 5-3-2013. Accessed: 2-7-2020.

[2] Gordon Gilmore. *Practical Gamma-Ray Spectrometry.* John Wiley & Sons, Ltd, 2rd edition, 2008.

[3] John Vagabond. How do photons interact with matter? simple scatter, compton scatter, pair production. `https://johnvagabondscience.wordpress.com/2014/04/14/how-photons-interact-with-matter/`, 14-04-2014. Accessed: 24-04-2020.

[4] Glenn F. Knoll. *Radiation Detection and Measurement, 3rd ed.* John Wiley and Sons, New York, 3rd edition, 2000.

[5] Gregory Gruber. A compact, discrete csi(tl) scintillator/si photodiode gamma camera for breast cancer imaging. 2000.

[6] Potassium 40. `https://www.radioactivity.eu.com/site/pages/Potassium_40.htm`. Accessed: 26-05-2020.

[7] Natural uranium. `https://www.nrc.gov/reading-rm/basic-ref/glossary/natural-uranium.html`, 21-05-2019. Accessed: 24-04-2020.

[8] Ronald Cornelius Gerardus Maria Smetsers and Roelf Onno Blaauboer. *Variations in Outdoor Radiation Levels in the Netherlands.* PhD thesis, 1996. date submitted: 2009 Rights: University of Groningen.

[9] Peter Hendriks, J Limburg, and RJ de Meijer. Full-spectrum analysis of natural gamma-ray spectra. *Journal of Environmental Radioactivity*, 53(3):365–380, 2001.

[10] International Atomic Energy Agency. Mapping Using Gamma Ray. *Encyclopedia of Atmospheric Sciences*, 4(July):1549–1555., 2003.

[11] Radioactive decay. `https://www.epa.gov/radiation/radioactive-decay`, 28-04-2019. Accessed: 4-07-2020.

[12] D. J. Strom and J. A. MacLellan. Evaluation of eight decision rules for low-level radioactivity counting. *Health Physics*, 81(1):27–34, 2001.

[13] J. Limburg R. Koomans M. Söderström S. de Waal S. van der Veeke, E.R. van der Graaf. Footprint and height corrections for uav-borne gamma-ray spectrometry studies. Unpublished manuscript.

[14] Marie-Martin Be, Venassa Chiste, C Dulieu, E Browne, C Baglin, V Chechev, N Kuzmenco, R Helmer, D MACMAHON, and K LEE. *Table of Radionuclides (Comments on evaluations)*, volume 7. 2004.

[15] Bai Li, Yi Zhu, Zhanyong Wang, Chao Li, Zhong Ren Peng, and Lixin Ge. Use of multi-rotor unmanned aerial vehicles for radioactive source search. *Remote Sensing*, 10(5), 2018.

[16] Han Limburg and Ronald Koomans. Ms-350 ultralight drone detectors. `https://the.medusa.institute/display/PD/MS-350+Ultralight+Drone+Detectors`. Accessed: 3-7-2020.

[17] F. J. Schima M. P. Unterweger, D. D. Hoppes and J. S. Coursey. Radionuclide half-life measurements data. `https://www.nist.gov/pml/radionuclide-half-life-measurements/radionuclide-half-life-measurements-data`, 15-11-2019. Accessed: 26-6-2020.

[18] DE McClain, AC Miller, and JF Kalinich. Status of Health Concerns about Military Use of Depleted Uranium and Surrogate Metals in Armor-Penetrating Munitions. *Afrri Cd*, pages 1–20, 2005.

[19] E. M. Lee, G. Menezes, and E. C. Finch. Natural radioactivity in building materials in the Republic of Ireland. *Health Physics*, 86(4):378–383, 2004.

[20] William Hughes, WAAS T&E Team, and Atlantic City International Airport. Global Positioning System (GPS) Standard Positioning Service (SPS) Performance Analysis Report FAA GPS Performance Analysis Report Executive Summary. (December 2016), 2017.

[21] Phantom 4 specs. `https://www.dji.com/nl/phantom-4/info`. Accessed: 3-7-2020.